Key Points:
- Eastern equatorial Pacific was less oxygen depleted during mid-Holocene despite warmer climate
- Orbitally driven mid-Holocene climate changes impact on ocean biogeochemistry
- Ocean physics dominate over ecology in driving mid-Holocene OMZ variability

Oxygen minimum zone variations in the tropical Pacific during the Holocene

Xu Xu[1], Joachim Segschneider[1], Birgit Schneider[1], Wonsun Park[2], and Mojib Latif[2]

[1]Institute of Geosciences, University of Kiel, Kiel, Germany, [2]GEOMAR Helmholtz Centre for Ocean Research Kiel, Kiel, Germany

Abstract We performed simulations with a global model of ocean biogeochemistry forced with orbitally driven anomalies of oceanic conditions for the mid-Holocene, known as Holocene climate optimum, to investigate natural variability in the eastern equatorial Pacific oxygen minimum zone (EEP OMZ). While the global mean temperature during the mid-Holocene was likely slightly higher than the 1961–1990 mean, the sea surface temperature in the EEP was slightly lower. Mid-Holocene oxygen concentrations in the EEP OMZ are generally increased, locally by up to 50%, and the EEP OMZ volume was, depending on definition of the OMZ threshold, at least 6% lower. These higher oxygen levels are the combined result of competing physical and biogeochemical processes. Our results imply that mechanisms for past changes in the EEP OMZ intensity and extension can differ from the global warming driven decline in oxygen levels observed for the recent decades and predicted for the future.

1. Introduction

The mid-Holocene, when summer insolation over the Northern Hemisphere and the seasonal cycle were stronger than present, is known as climate optimum during the Holocene. Global mean climate has been estimated to be 0.4 K warmer than the 1961–1990 mean [*Marcott et al.*, 2013]. Northern Hemisphere temperatures were higher than today in summer, and lower in winter, whereas Southern Hemisphere temperatures changed less. Substantial regional variations in various climate parameters have been recorded in proxies [*Mayewski et al.*, 2004; *Leduc et al.*, 2010] and model simulations [*Zheng et al.*, 2008; *Schneider et al.*, 2010]. These imply slightly lower tropical and eastern equatorial Pacific (EEP) sea surface temperatures (SSTs) during the mid-Holocene, in line with more intense upwelling and more La Niña like conditions. The goal of this study is to simulate the mean state of the EEP oxygen minimum zone (OMZ) during the mid-Holocene and to identify the mechanisms that drive the changes compared to preindustrial conditions and global warming related changes.

In well ventilated surface waters oxygen concentrations are generally high, that is close to saturation value. In the ocean interior, oxygen is consumed by aerobic respiration of particulate organic matter. As a result of this consumption, OMZs have formed in areas of high biological production in which the oxygen supply by currents is weak. These OMZs are typically located between 100 and 900 m depth [*Karstensen et al.*, 2008] in upwelling areas such as the EEP and in the Arabian Sea, and, to less extent, in the tropical Atlantic.

Observations indicate a widespread warming of the global ocean since the mid-1950s [*Levitus et al.*, 2000]. Expanding and intensifying OMZs have likewise been observed in the tropical Pacific, Indian, and Atlantic Oceans [*Stramma et al.*, 2008]. This expansion has been related to the observed global warming but also to more regional climate variations, e.g., for the EEP to changes in the Pacific Decadal Oscillation [*Czeschel et al.*, 2012]. Model studies based on future emission scenarios of fossil fuel carbon dioxide predict a further modest growth and intensification of OMZs as global warming continues [*Matear and Hirst*, 2003; *Cocco et al.*, 2013; *Bopp et al.*, 2013].

The extension and intensity of the OMZs is the result of complex interactions of climate, ocean currents, and biogeochemistry [*Moffitt et al.*, 2015]. Here we investigate if orbitally driven changes in climate during the mid-Holocene result in significantly changed oxygen concentrations in the EEP OMZ and which processes would drive such changes.

2. Methods

We use results from a standard Paleoclimate Modeling Intercomparison Project (PMIP) [*Joussaume and Taylor*, 1995] experiment with a global coupled atmosphere-ocean-sea ice model (the Kiel Climate Model, KCM) [*Park and Latif*, 2008; *Park et al.*, 2009] and from Nucleus for European Modelling of the Ocean (NEMO) [*Madec*, 2008], which also serves as oceanic component of KCM, in off-line mode to force a global model of the marine biogeochemistry (Pelagic Interaction Scheme for Carbon and Ecosystem Studies, PISCES) [*Aumont et al.*, 2003].

KCM has been used to conduct and analyze simulations of the preindustrial and the mid-Holocene climate [*Schneider et al.*, 2010; *Khon et al.*, 2010, 2012; *Salau et al.*, 2012]. Orbital parameters (eccentricity, obliquity, and precession) were varied as forcing according to the standard protocol of PMIP [*Braconnot et al.*, 2008]. The greenhouse gas concentrations were set to preindustrial levels for both KCM simulations according to the PMIP protocol, and the ice sheet impact is neglected.

The ocean component (Océan PArallélisé) uses a tripolar grid with 2° zonal resolution and a meridional resolution varying from 0.5° at the equator to 2° × cos(latitude) poleward of 20°. The water column is divided into 31 layers, with 20 layers in the upper 500 m. OPA in this configuration has been shown to give a reasonable representation of the equatorial current system in the Pacific, while some currents that transport oxygen-rich waters to the EEP below the depth of the eastward equatorial undercurrent (EUC), like the Tsuchiya jets, remain poorly resolved [*Rodgers et al.*, 2003]. ECHAM5 the atmospheric component of KCM, is run in T31 resolution with 19 layers.

2.1. Marine Biogeochemistry Model

PISCES [*Aumont et al.*, 2003] simulates the marine biogeochemistry including processes that determine dissolved oxygen concentrations based on the oceanic circulation as provided by NEMO [*Madec*, 2008] and a nutrient-phytoplankton-zooplankton-detritus type description of the marine ecosystem. Here we restrict the description of PISCES to the processes relevant for the oxygen concentration. Sources of oxygen are gas exchange with the atmosphere at the surface and biological production in the euphotic zone. Oxygen is consumed by respiration of organic matter over the whole water column.

The production of two phytoplankton groups (representing nanophytoplankton and diatoms) is simulated based on temperature, the availability of light, and the nutrients P, N (both as nitrate and ammonium), Si (for diatoms), and the micronutrient Fe. The elemental ratios of iron, chlorophyll, and silicate within diatoms are computed prognostically based on the surrounding water's concentration of nutrients; otherwise, they are constant following the Redfield ratios.

There are three nonliving components of organic carbon in PISCES: semilabile dissolved organic carbon (DOC), as well as large and small particulate organic carbon (POC), which are fueled by mortality, aggregation, fecal pellet production, and grazing. Large and small POC sinks to the sea floor with their respective settling velocities of 2 and 50 m d^{-1}. Remineralization of DOC and POC is simulated over the whole water column. The rate depends on temperature with a Q_{10} of 1.8 and on the oxygen level, with a reduced rate for O_2 concentrations below 6 µmol L^{-1}.

2.2. Experiments

We perform two off-line experiments with PISCES for this study, one for preindustrial conditions (0k) and one for mid-Holocene conditions (6k). Both experiments are integrated to steady state over more than 5000 years using constant ocean fields retaining the seasonal cycle. For the preindustrial simulation the ocean fields are obtained from the stand alone NEMO ocean-sea ice model forced by climatological atmospheric boundary conditions from National Centers for Environmental Prediction (NCEP)/National Center for Atmospheric Research [*Kalnay et al.*, 1996].

To force the mid-Holocene experiment, anomalies of oceanic conditions are added to the preindustrial oceanic state. One hundred year averages retaining the seasonal cycle of the oceanic anomaly fields from NEMO for the KCM mid-Holocene experiment were added to the fields of the NCEP-forced NEMO preindustrial simulation to drive the 6k experiment of the marine biogeochemistry. Atmospheric oxygen concentrations are constant at a present day value in both experiments.
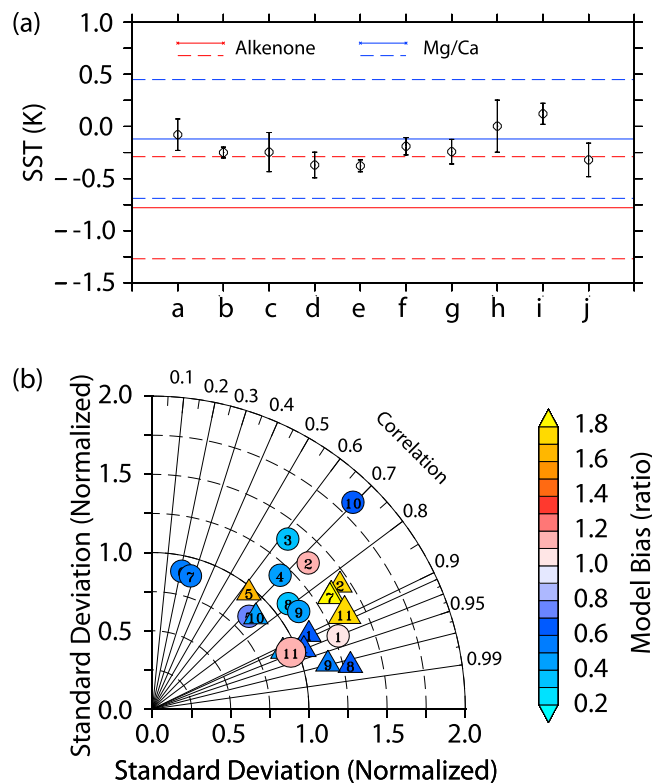
Figure 1. (a) Simulated and proxy-based estimates of the EEP SST anomaly (K) during the mid-Holocene. Proxy-based estimates (solid lines) for Alkenones (red) and Mg/Ca (blue) and their uncertainty range (dashed, +/− 1 standard deviation) from *Leduc et al.* [2010]. Model estimates from various PMIP models: a = CNRM-CM5, b = CSIRO-MK3-6-0, c = IPSL-CM5A-LR, d = MRI-CGM3, e = BCC-CSM1.1, f = CCSM4, g = CSIRO-MK3L-1-2, h = GISS-E2-R, i = HadGEM2-ES, and j = KCM. (b) Taylor diagram for present-day annual mean O_2 concentration ($\mu mol\ L^{-1}$] computed over 125°W–80°W, 20°–20°N for the whole water column (circles) and 200 m to 600 m depth (triangles). Observations are taken from World Ocean Atlas (WOA) 2009 [*Garcia et al.*, 2010]. The color shading shows the bias between the observations and the modeled data as a ratio (1 = no bias). 1 = CESM1-BGC, 2 = CMCC-ESM, 3 = GFDL-ESM2G, 4 = GFDL-ESM2M, 5 = HadGEM2-ES, 6 = IPSL-CM5A-LR, 7 = IPSL-CM5A-MR, 8 = MPI-ESM-LR, 9 = MPI-ESM-MR, 10 = NorESM1-ME, 11 = PISCES forced by NEMO 0k as employed in this study.

3. Results

Our analysis is focused on the EEP, where the globally largest OMZ is presently observed and where proxy-based estimates of temperature change exist [*Leduc et al.*, 2010] and proxies for marine biogeochemistry are emerging [*Moffitt et al.*, 2015].

3.1. Holocene SST Trends in the EEP

KCM-derived mid-Holocene SSTs for an area from 10°S–10°N, 95°W–80°W are compared with proxy data and PMIP models in Figure 1a. The proxy data are SST reconstructions from alkenone unsaturation values $UK^{K'}_{37}$ and Mg/Ca ratios [*Leduc et al.*, 2010]. The proxy-derived Holocene SST trends are calculated as the difference between the first and the last 1000 years in the proxy records and assumed to be linear. A detailed description of the data set is given by *Leduc et al.* [2010] and a detailed comparison with KCM data in *Schneider et al.* [2010]. Model results are from the PMIP models listed in the caption of Figure 1a.

In the KCM mid-Holocene simulation the SST in the EEP is lower than preindustrial by around 0.3 K (model "j" to the far right in Figure 1a). This is in the range of PMIP model results, and in the uncertainty range of, but slightly stronger than, the Mg/Ca proxy-based estimate of a cooling by 0.1 K ± 0.6 K. It is weaker than the Alkenone-based estimate of about −0.8 K but still on the very margin of its uncertainty range.

3.2. Validation of Preindustrial Oxygen

To validate the simulated preindustrial oxygen fields, these are compared in a Taylor diagram to observations from WOA 2009 [*Garcia et al.*, 2010] and results from several models from the Climate Model
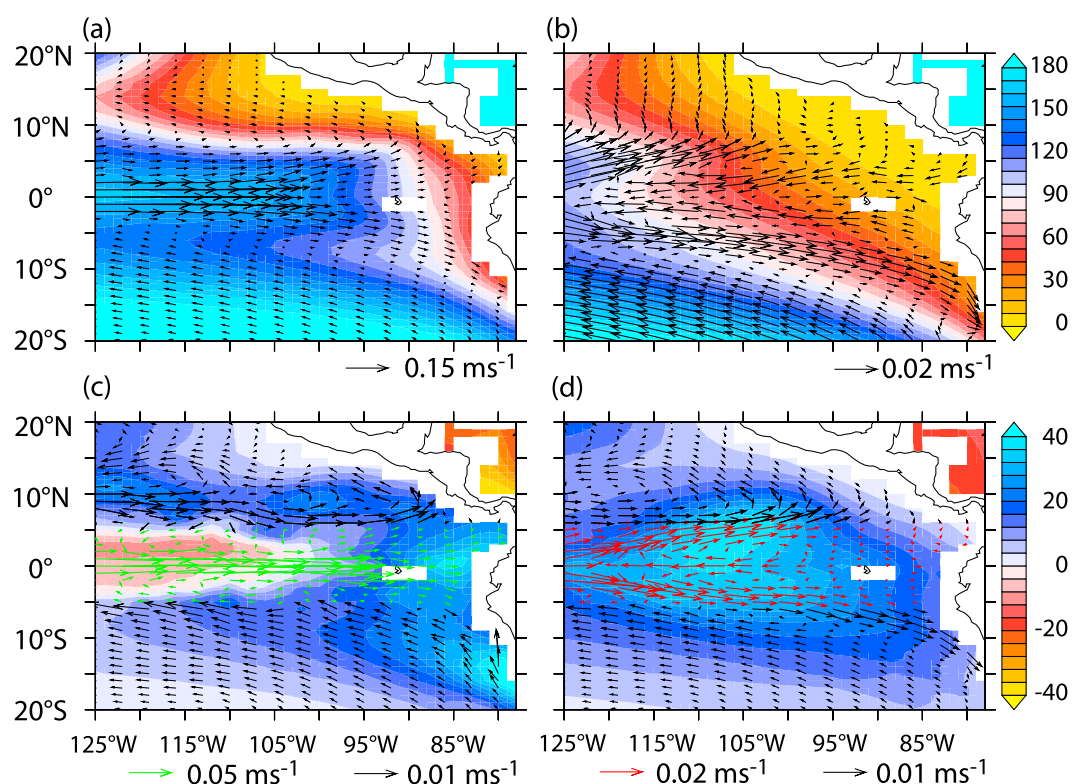
Figure 2. Model results for simulated present day O_2 concentration (shading, μmol L^{-1}) and velocity field (arrows, m s^{-1}) at (a) $\sigma_\theta = 26.0$ kg m^{-3} and (b) $\sigma_\theta = 26.5$ kg m^{-3} and mid-Holocene change in O_2 concentration (shading) and change in velocity field (arrows, note different scaling vectors) for (c) $\sigma_\theta = 26.0$ kg m^{-3} and (d) $\sigma_\theta = 26.5$ kg m^{-3}.

Intercomparison Project phase 5 (CMIP5). The Taylor diagram (Figure 1b) is based on oxygen concentrations between 125°W–80°W and 20°–20°N. Circles indicate values for the whole water column, triangles over 200 m–600 m depth mean. The oxygen field of PISCES forced by NEMO (model 11) agrees with observations from WOA 2009 in the same range as the CMIP5 Earth system models (model names are listed in the caption of Figure 1b). The spatial correlation of the NEMO-forced PISCES O_2 concentrations with the WOA data is quite high at around 0.93. The simulated variability is similar to the observed one for the whole water column and higher for the 200–600 m depth range (by a factor of around 1.35). Simulated oxygen levels are biased toward too much oxygen by a factor of 1.1 for the whole water column and by a factor of 1.7 for the 200 m to 600 m depth range. Despite these deviations, we consider the present day oxygen fields that form the basis of our study of sufficient quality within the limitations of the current state of the art , but it must be emphasized that basically all current state-of-the-art models suffer from either high or low biases.

3.3. Preindustrial and Mid-Holocene O_2 and Flow Field in the EEP
We first investigate the simulated oxygen fields on two σ levels. $\sigma_\theta = 26.0$ kg m^{-3} (henceforth σ_{26}) represents the upper boundary of the EEP OMZ at around 100 m to 120 m depth on the equator depending on longitude, and up to 300 m depth depending on latitude, a depth range for which emerging proxy records of δ^{15}N are most representative. The $\sigma_\theta = 26.5$ kg m^{-3} level (henceforth $\sigma_{26.5}$) is at around 250 m to 300 m depth at the equator, near the depth of the center of the OMZ, and where the strongest changes in O_2 are simulated for the mid-Holocene.

On σ_{26} (Figure 2a), the EEP OMZ for the 90 μmol L^{-1} threshold extends westward to 120°W north of the equator centered at around 15°N even at this shallow level (see also isopycnals in Figure 3 for an indication of their depths). A weak westward down-gradient (with respect to oxygen) current favors low oxygen concentrations in this area. South of around 8°N the eastward equatorial undercurrent (EUC), which is centered on the equator, transports water with higher oxygen concentrations from the central Pacific into the EEP. As a result, oxygen concentrations are above OMZ levels despite the high biological production and export near
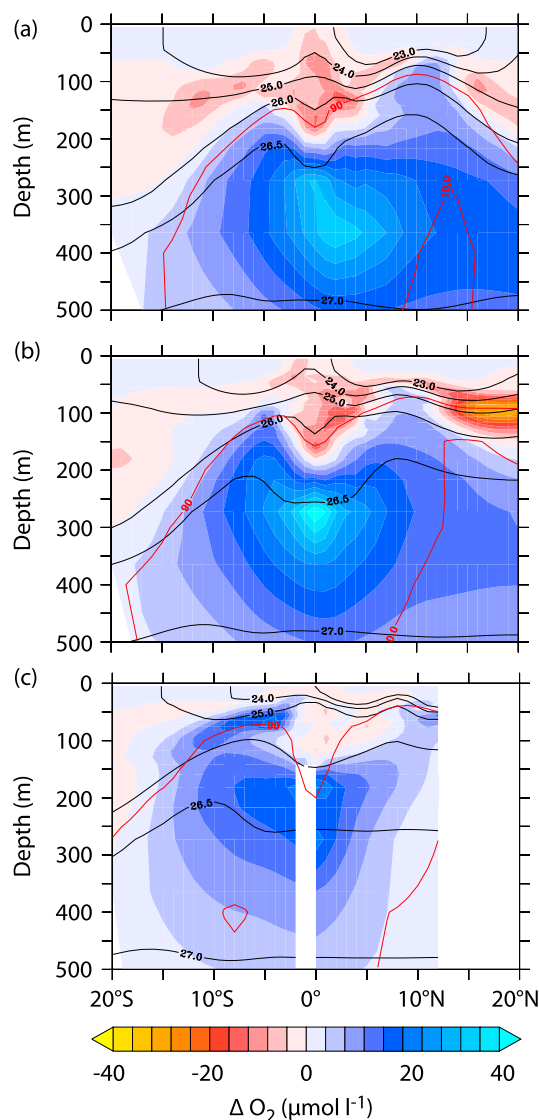
Figure 3. Simulated mid-Holocene change (6k–0k) in O_2 concentration ($\mu mol\ L^{-1}$) for meridional sections along (a) 125°W, (b) 110° W, and (c) 90°W. Red contour lines indicate O_2 concentrations of 10 and 90 $\mu mol\ L^{-1}$ and represent suboxic zones and the outer boundary of the OMZ, respectively.

the equator (see also Figure 4). South of the equator, low oxygen concentrations are confined to a narrow band close to the coast.

On $\sigma_{26.5}$ (Figure 2b) the OMZ is much larger than at σ_{26} in agreement with observations [*Garcia et al.*, 2010]. For the 90 $\mu mol\ L^{-1}$ threshold, the OMZ extends to the west as far as 140°W and is more intense north of the equator where the flow field is generally quite sluggish north of 5°N (Figure 2b). In the vicinity of the equator, westward currents transport oxygen-depleted waters away from the center of the OMZ but east of 110°W a locally confined eastward current sets in the opposite direction. South of the equator, between 5°S and 10°S, eastward inflow weakens the OMZ, and further south oxygen concentrations are well above OMZ levels due to inflow from the south-east.

During the mid-Holocene (Figure 2c) O_2 concentrations at σ_{26} in the low oxygen zones are increased by up to 40 $\mu mol\ L^{-1}$ mainly in two zonal bands centered at 10°N and 10°S and in two regions near the coast, one on the equator and one at 15°S. This can be attributed to an increased transport of waters with higher oxygen concentration into the low oxygen regions (arrows in Figure 2c, note different scaling vectors). North of the equator, these waters come from the more western Pacific. At 10°S, off the coast of Peru, oxygen concentrations are increased by more than 30 $\mu mol\ L^{-1}$. In this area, a stronger inflow from the southeast and reduced primary production (Figure 4) result in higher oxygen levels. In the vicinity of the equator oxygen concentrations on σ_{26} are lower during the mid-Holocene mainly west of 100°W. This is in spite of an intensified EUC (green arrows) and must, therefore, be caused by a combination of intensified upwelling (lifting the O_2 profile, which displays decreasing oxygen concentrations with depth at this level) and the increased biological production in this area during the mid-Holocene (see Figure 4).

On $\sigma_{26.5}$ (Figure 2d) oxygen concentrations in the EEP are generally increased during the mid-Holocene. This increase is up to 12 $\mu mol\ L^{-1}$ near the coast where oxygen concentrations are lowest. A larger increase of up to 40 $\mu mol\ L^{-1}$ is simulated further to the west near the equator, still within the OMZ. These changes are clearly linked to the flow field as seen by the anomaly vectors in Figure 2d. The changes in the flow field can be described by a northward shift by 2–3° of the mainly zonal currents shown in Figure 2b, resulting in a stronger inflow of less oxygen depleted waters from the west into the OMZ.
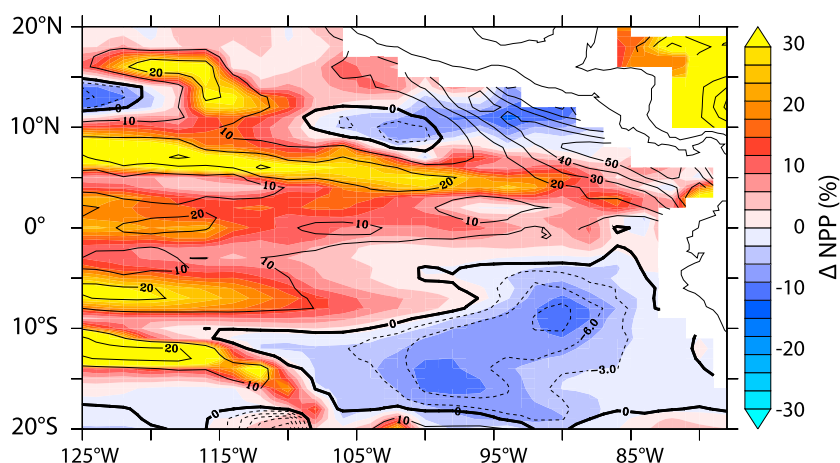
Meridional sections at 125°W, 110°W, and 90°W show further details of the spatial structure of the changes in oxygen concentration between mid-Holocene and preindustrial for the upper 500 m in the EEP (Figure 3). In all sections an increase of oxygen concentrations (bluish) is seen in the OMZ as defined by the 90 $\mu mol\ L^{-1}$ threshold (indicated by the corresponding red contour line). The maximum increase is centered in the upper part of the OMZ. Changes in the suboxic part of the OMZ as indicated by the 10 $\mu mol\ L^{-1}$ contour line are smaller in absolute terms but can be quite large in comparison to the preindustrial values. All three sections

Figure 4. Simulated change in percent between mid-Holocene and preindustrial (6k−0k) for integrated primary production (shading) and POC flux attenuation between 200 m and 500 m (contour lines, contour interval is 10% for positive and 3% for negative anomalies).

also exhibit a band of decreased oxygen concentrations in the upper water column that, however, only partly overlaps with the OMZ even as defined by the uppermost threshold of 90 μmol L^{-1}.

Figure 4 shows that the integrated primary production (shading) is higher in the mid-Holocene than preindustrial in most of the EEP near the equator by up to 30% and lower by up to 15% in two regions off the Americans' coast, centered at around 10° latitude on both hemispheres. These productivity changes are driven by redistributions of nutrients near the surface (identical pattern, not shown) and result in corresponding reductions in POC flux attenuation between 200 m and 500 m depth (Figure 4, contour lines), indicating lower oxygen consumption by POC respiration in this area and depth range.

4. Discussion and Conclusions

Although the mid-Holocene global climate was moderately warmer than the preindustrial one, the simulated O$_2$ concentrations were up to 50% higher in the EEP OMZ and up to 100% higher in suboxic zones. This raises the question, if the recently observed declines in oxygen levels that have been attributed to global warming and the further reduction predicted for the future as global warming continues are at odds with our results, or if different mechanisms can be identified that explain the seemingly contradicting results.

In our model simulation, the main mechanism that causes increased oxygen concentrations in the mid-Holocene is a local shift and intensification of the ocean currents that provide oxygen to the EEP. In KCM, the Intertropical Convergence Zone (ITCZ) is shifted northward during the mid-Holocene [*Khon et al.*, 2012; *Salau et al.*, 2012] and this drives a northward shift of the nonequatorially confined zonal currents in the tropical Pacific, leading to higher transport of oxygen into the EEP OMZ. Source regions of the EUC waters cover a vast range of the Pacific ocean, with rather little direct meridional inflow from near the equator [*Rodgers et al.*, 2003]. It has been stated that the ITCZ forms a potential vorticity barrier for direct meridional transport into the equatorial region [*Lu and McCreary*, 1995], and therefore, the northward shift of the ITCZ would potentially change the source regions of EUC waters. In our simulations, oxygen concentrations in the EUC region west of the OMZ are lower during the mid-Holocene (Figure 2c) mainly due to higher export production. But the oxygen concentrations are still much higher than in the OMZ, and, therefore, the intensified EUC results in enhanced oxygen supply to the OMZ.

The enhanced oxygen supply by currents has a stronger impact on the oxygen concentrations than the increased primary production and oxygen consumption by remineralization on and near the equator. Locally decreased POC flux attenuation, as off Peru, and the corresponding reduction of oxygen consumption additionally cause increased oxygen concentrations, and this agrees with relatively low marine sedimentation rates and low productivity during the mid-Holocene in this area [*Makou et al.*, 2010; *Rein et al.*, 2005].

Our results are in-line with previous studies indicating that the extension of oxygen depleted water volumes is mainly controlled by ocean dynamics rather than by local biological production and remineralization

[*Meissner et al.*, 2005; *Galbraith et al.*, 2004]. Various studies suggest a general cooling of the sea surface in the EEP during the mid-Holocene, potentially driven by stronger upwelling in this area [*Luan et al.*, 2012; *Carré et al.*, 2011; *Koutavas and Sachs*, 2008; *Kienast et al.*, 2006; *Koutavas et al.*, 2006; *Loubere et al.*, 2003]. Stronger trade winds intensify upwelling on the equator—driving higher primary production—and cause a larger zonal sea level gradient across the equatorial Pacific that drives, in turn, a stronger EUC as seen also in the simulation presented here.

In the mid-Holocene, oxygen concentrations are higher than preindustrial mainly in the upper part of the EEP OMZ as defined by the 90 μmol L^{-1} threshold. Here the impact of oxygen supply on higher trophic levels is likely to be largest. The total volume of the EEP OMZ is 6% smaller in the mid-Holocene. In the currently suboxic zones, at O$_2$ concentrations below 10 μmol L^{-1}, the trend over the Holocene is quite large in relative numbers (Figures 3a–3c).

It must be noted that current state-of-the-art models that are employed to simulate the world's OMZ still suffer from limitations yet to be overcome. One issue is ocean model resolution, which is generally still too coarse to resolve the equatorial and near-coastal current system with sufficient accuracy. Coupled models including KCM, frequently simulate a double ITCZ, show an equatorial cold bias and EEP warm bias and thus wrong properties of thermostat waters due to the Bjerknes feedback, cloud cover-SST feedback, and poor representation of tropical instability waves [*Park et al.*, 2009]. Mismatches in upwelling and lateral currents cause errors in the nutrient supply to the euphotic layer and therefore in biological production, export, and oxygen consumption by remineralization. Next to the physical limitations, the description of the marine ecosystem including the remineralization of organic matter is still simplified in all models. Overall, models should be improved in resolution and the representation of physical and biogeochemical processes.

The processes that drive OMZ changes may well be different for past—orbitally driven—climate variations than for the more globally uniform recent warming driven by increasing greenhouse gas concentrations [see also *Moffitt et al.*, 2015]. The main mechanism that drives the changes in the 21st century model simulations is a slower mixing of oxygen to deeper levels as the ocean is more stably stratified in a warmer climate, whereas solubility changes are of minor importance and partly compensated by reduced biological production [*Matear and Hirst*, 2003; *Cocco et al.*, 2013; *Bopp et al.*, 2013]. According to our simulation, orbitally driven alterations of the OMZ near circulation result in OMZ variations contrary to those expected from global warming simulations.

References

Aumont, O., E. Maier-Reimer, S. Blain, and P. Monfray (2003), An ecosystem model of the global ocean including Fe, Si, P colimitations, *Global Biogeochem. Cycles*, *17*(2), 1060, doi:10.1029/2001GB001745.

Bopp, L., et al. (2013), Multiple stressors of ocean ecosystems in the 21st century: Projections with CMIP5 models, *Biogeosciences*, *10*(10), 6225–6245, doi:10.5194/bg-10-6225-2013.

Braconnot, P., C. Marzin, L. Grégoire, E. Mosquet, and O. Marti (2008), Monsoon response to changes in Earth's orbital parameters: Comparisons between simulations of the Eemian and of the Holocene, *Clim. Past*, *4*(4), 281–294, doi:10.5194/cp-4-281-2008.

Carré, M., M. Azzoug, I. Bentaleb, B. M. Chase, M. Fontugne, D. Jackson, M. P. Ledru, A. Maldonado, J. P. Sachs, and A. J. Schauer (2011), Mid-Holocene mean climate in the south eastern Pacific and its influence on South America, *Quat. Int.*, *253*, 55–66, doi:10.1016/j.quaint.2011.02.004.

Cocco, V., et al. (2013), Oxygen and indicators of stress for marine life in multi-model global warming projections, *Biogeosciences*, *10*, 1849–1868.

Czeschel, R., L. Stramma, and G. C. Johnson (2012), Oxygen decreases and variability in the eastern equatorial Pacific, *J. Geophys. Res.*, *117*, C11019, doi:10.1029/2012JC008043.

Galbraith, E. D., M. Kienast, T. F. Pedersen, and S. E. Calvert (2004), Glacial-interglacial modulation of the marine nitrogen cycle by high-latitude O$_2$ supply to the global thermocline, *Paleoceanography*, *19*, PA4007, doi:10.1029/2003PA001000.

Garcia, H. E., R. A. Locarnini, T. P. Boyer, J. I. Antonov, O. K. Baranova, M. M. Zweng, and D. R. Johnson (2010), World Ocean Atlas 2009, Volume 3: Dissolved oxygen, apparent oxygen utilization, and oxygen saturation, in *NOAA Atlas NESDIS 70*, edited by S. Levitus, 344 pp., U.S. Gov. Print. Off., Washington, D. C.

Joussaume, S., and K. E. Taylor (1995), Status of the Paleoclimate Modeling Intercomparison Project (PMIP), in *Proceedings of the First International AMIP Scientific Conference*, vol. 92, edited by W. L. Gates, pp. 42–430, World Clim. Res. Programme, Geneva, Switzerland.

Kalnay, E., et al. (1996), The NCEP/NCAR 40-year reanalysis project, *Bull. Am. Meteorol. Soc.*, *77*, 437–471.

Karstensen, J., L. Stramma, and M. Visbeck (2008), Oxygen minimum zones in the eastern tropical Atlantic and Pacific oceans, *Prog. Oceanogr.*, *77*, 331–350.

Khon, V. C., W. Park, M. Latif, I. I. Mokhov, and B. Schneider (2010), Response of the hydrological cycle to orbital and greenhouse gas forcing, *Geophys. Res. Lett.*, *37*, L19705, doi:10.1029/2010GL044377.

Khon, V. C., W. Park, M. Latif, I. I. Mokhov, and B. Schneider (2012), Tropical circulation and hydrological cycle response to orbital forcing, *Geophys. Res. Lett.*, *39*, L15708, doi:10.1029/2012GL052482.

Kienast, M., S. S. Kienast, S. E. Calvert, T. I. Eglinton, G. Mollenhauer, R. François, and A. C. Mix (2006), Eastern Pacific cooling and Atlantic overturning circulation during the last deglaciation, *Nature*, *443*, 846–849, doi:10.1038/nature05222.

Koutavas, A., and J. P. Sachs (2008), Northern timing of deglaciation in the eastern equatorial Pacific from alkenone paleothermometry, *Paleoceanography*, *23*, PA4205, doi:10.1029/2008PA001593.

Koutavas, A., P. B. deMenocal, G. C. Oliver, and J. Lynch-Stieglitz (2006), Mid-Holocene El Niño-Southern Oscillation (ENSO) attenuation revealed by individual foraminifera in eastern tropical Pacific sediments, *Geology*, *34*(12), 993–996, doi:10.1130/G22810A.1.

Leduc, G., R. Schneider, J. H. Kim, and G. Lohmann (2010), Holocene and Eemian sea surface temperature trends as revealed by alkenone and Ma/Ca paleothermometry, *Quat. Sci. Rev.*, *29*, 989–1004.

Levitus, S., J. I. Antonov, T. P. Boyer, and C. Stephens (2000), Warming of the world ocean, *Science*, *287*, 2225–2229, doi:10.1126/science.287.5461.2225.

Loubere, P., M. Richaud, Z. Y. Liu, and F. Mekik (2003), Oceanic conditions in the eastern equatorial Pacific during the onset of ENSO in the Holocene, *Quat. Res.*, *60*, 142–148.

Lu, P., and P. McCreary Jr. (1995), Influence of the ITCZ on the flow of thermocline water from the subtropical to the equatorial Pacific Ocean, *J. Phys. Oceanogr.*, *25*, 3076–3088.

Luan, Y., P. Braconnot, Y. Yu, W. Zheng, and O. Marti (2012), Early and mid-Holocene climate in tropical Pacific: Seasonal cycle and interannual variability induced by insolation changes, *Clim. Past*, *8*, 1093–1108, doi:10.5194/cp-8-1093-2012.

Madec, G. (2008), NEMO ocean engine, *Note du Pôle de Modélisation 27*, Inst. Pierre–Simon Laplace. Paris.

Makou, M. C., T. L. Eglinton, D. W. Oppo, and K. A. Hughen (2010), Postglacial changes in El Niño and La Niña behavior, *Geology*, *38*, 43–46.

Marcott, S., J. D. Shakun, P. Clark, and A. Mix (2013), A reconstruction of regional and global temperature for the past 11,300 years, *Science*, *339*, 1189–1201, doi:10.1126/science.1228026.

Matear, R. J., and C. Hirst (2003), Long-term changes in dissolved oxygen concentrations in the ocean caused by protracted global warming, *Global Biogeochem. Cycles*, *17*(4), 1125, doi:10.1029/2002GB001997.

Mayewski, P. A., et al. (2004), Holocene climate variability, *Quat. Res.*, *62*, 243–255.

Meissner, K. J., E. D. Galbraith, and C. Völker (2005), Denitrification under glacial and interglacial conditions: A physical approach, *Paleoceanography*, *20*, PA3001, doi:10.1029/2004PA001083.

Moffitt, S. E., R. A. Moffitt, W. Sauthoff, C. V. Davis, K. Hewett, and T. M. Hill (2015), Paleoceanographic insights on recent oxygen minimum zone expansion: Lessons for modern oceanography, *PLoS ONE*, *10*, e0115246, doi:10.1371/journal.pone.0115246.

Park, W., and M. Latif (2008), Multidecadal and multicentennial variability of the meridional overturning circulation, *Geophys. Res. Lett.*, *35*, L22073, doi:10.1029/2008GL035779.

Park, W., N. Keenlyside, M. Latif, A. Ströh, R. Redler, E. Roeckner, and G. Madec (2009), Tropical Pacific climate and its response to global warming in the Kiel Climate Model, *J. Clim.*, *22*, 71–92, doi:10.1175/2008JCLI2261.1.

Rein, B., A. Lückge, L. Reinhard, F. Sirocko, A. Wolf, and W. C. Dullo (2005), El Niño variability off Peru during the last 20,000 years, *Paleoceanography*, *20*, PA4003, doi:10.1029/2004PA001099.

Rodgers, K., B. Blanke, G. Madec, O. Aumont, P. Ciais, and J. Dutay (2003), Extratropical sources of equatorial Pacific upwelling in an OGCM, *Geophys. Res. Lett.*, *30*(2), 1084, doi:10.1029/2002GL016003.

Salau, O. R., B. Schneider, W. Park, V. Khon, and M. Latif (2012), Modeling the ENSO impact of orbitally induced mean state climate changes, *J. Geophys. Res.*, *117*, C05043, doi:10.1029/2011JC007742.

Schneider, B., G. Leduc, and W. Park (2010), Disentangling seasonal signals in Holocene climate trends by satellite-model-proxy integration, *Paleoceanography*, *25*, PA4217, doi:10.1029/2009PA001893.

Stramma, L., G. C. Johnson, J. Sprintall, and V. Mohrholz (2008), Expanding oxygen minimum zones in the tropical oceans, *Science*, *320*, 655–685.

Zheng, W., P. Braconnot, E. Guilyardi, U. Merkel, and Y. Yu (2008), ENSO at 6ka and 21ka from ocean-atmosphere coupled model simulations, *Clim. Dyn.*, *321*, 745–762, doi:10.1007/s00382-007-0320-3.